We are IntechOpen,
the world's leading publisher of
Open Access books
Built by scientists, for scientists

4,800
Open access books available

122,000
International authors and editors

135M
Downloads

Our authors are among the

154
Countries delivered to

TOP 1%
most cited scientists

12.2%
Contributors from top 500 universities

CLARIVATE ANALYTICS
BOOK CITATION INDEX
INDEXED

WEB OF SCIENCE™

Selection of our books indexed in the Book Citation Index
in Web of Science™ Core Collection (BKCI)

Interested in publishing with us?
Contact book.department@intechopen.com

Numbers displayed above are based on latest data collected.
For more information visit www.intechopen.com

Limits in Planar PIV Due to Individual Variations of Particle Image Intensities

Holger Nobach
Max Planck Institute for Dynamics and Self-Organization
*Germany*

1. Introduction

The basic algorithm of digital particle image velocimetry (PIV) processing (Keane & Adrian, 1992; Utami et al., 1991; Westerweel, 1993; Willert & Gharib, 1991) utilizes the cross-correlation of image sub-spaces (interrogation windows) for local displacement estimation from two consecutively acquired images of a tracer-particle-laden flow. A variety of image processing techniques using sub-pixel interpolations has been applied in the past to significantly improve both, the accuracy of the particle displacement measurement beyond the nominal resolution of the optical sensor and the spatial resolution beyond the nominal averaging size of image sub-spaces to be correlated. These include:

- sub-pixel interpolation of the correlation planes, e.g. the peak centroid (center-of-mass) method (Alexander & Ng, 1991; Morgan et al., 1989), the Gaussian interpolation (Willert & Gharib, 1991), a sinc interpolation (Lourenco & Krothapalli, 1995; Roesgen, 2003) or a polynomial interpolation (Chen & Katz, 2005), which reduce the "pixel locking" or "peak locking" effect (Christensen, 2004; Fincham & Spedding, 1997; Lourenco & Krothapalli, 1995; Prasad et al., 1992; Westerweel, 1998)

- windowing functions, vanishing at the interrogation window boundaries (Gui et al., 2000; Liao & Cowen, 2005), reducing the effect of particle image truncation at the edges of the interrogation windows to be correlated (Nogueira et al., 2001; Westerweel, 1997)

- direct correlation with a normalization, which so far has been realized in three ways: asymmetrically, with a small interrogation window from the first image correlated with a larger window in the second image (Fincham & Spedding, 1997; Huang et al., 1997; 1993a; Rohály et al., 2002), symmetrically, with two interrogation windows of the same size (Nobach et al., 2004; Nogueira et al., 1999) or bi-directional, combining an asymmetric direct correlation as above and a second direct correlation with a small interrogation window from the second image correlated with a larger window in the first image (Nogueira et al., 2001), originally introduced as a "symmetric" method, but nonetheless using image sub-spaces of different sizes

- iterative shift and deformation of the interrogation windows (Fincham & Delerce, 2000; Huang et al., 1993b; Lecordier, 1997; Scarano, 2002; Scarano & Riethmuller, 2000) with different image interpolation schemes as e.g. the widely used, bi-linear interpolation, or more advanced higher-order methods (Astarita, 2006; Astarita & Cardone, 2005; Chen & Katz, 2005; Fincham & Delerce, 2000; Lourenco & Krothapalli, 1995; Roesgen, 2003)

including the Whittaker interpolation (Scarano & Riethmuller, 2000; Whittaker, 1929), also known as sinc or cardinal interpolation and the bi-cubic splines, which have found wide acceptance

- image deformation techniques (Astarita, 2007; 2008; Jambunathan et al., 1995; Lecuona et al., 2002; Nogueira et al., 1999; Nogueira, Lecuona & Rodriguez, 2005; Nogueira, Lecuona, Rodriguez, Alfaro & Acosta, 2005; Scarano, 2004; Schrijer & Scarano, 2008; Tokumaru & Dimotakis, 1995), where the entire images are deformed accordingly to the assumed velocity field before the sub-division into interrogation windows to be correlated, also using different image interpolation techniques.

With iterative window shift and deformation or image deformation techniques, an accuracy of the order of 0.01 pixel or better has been reported (Astarita & Cardone, 2005; Lecordier, 1997; Nobach et al., 2005) based on synthetic test images. In contrast, the application to real images from experiments shows less optimistic results, where the limit usually observed is about 0.1 pixel. Only under special conditions, like in two-dimensional flows with carefully aligned light sheets, can better accuracy be achieved (Lecordier & Trinité, 2006).
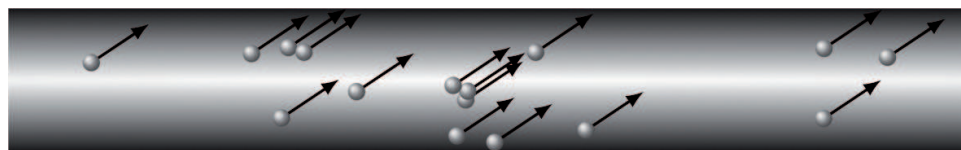
(a) Particles having an out-of-plane velocity component
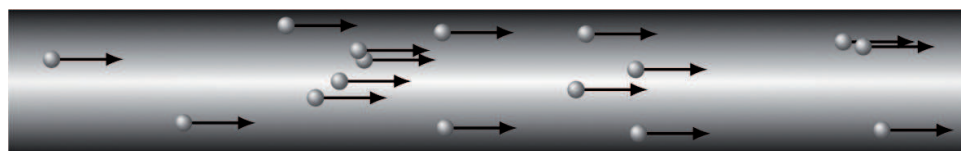
(b) Two-dimensional flow aligned with the light sheet plane (only in-plane velocity components)

Fig. 1. Particles moving through a light sheet with an intensity profile

One reason for the different achievable accuracies in simulations and experiments may be the fact that in experiments, particles usually change their position within the light sheet (Fig. 1a). Therefore, the particles are illuminated differently in the two consecutive exposures. Additionally, the different illumination is individually different for each particle due to their different starting positions perpendicular to the light sheet plane. The result is an individual variation of particle intensities (further denoted as "intensity variations"), even in a homogeneous flow without any velocity gradient. Intensity variations can easily be seen in images from a variety of PIV applications, where some particles become brighter between the two exposures, whereas other particles, even if close by, become darker (Fig. 2). Simulations often assume that different particles can have different intensities, but not that the intensities can vary between subsequent exposures. This scenario can be realized in experiments only in two-dimensional flows with light sheets exactly aligned parallel to the flow field (Fig. 1b). Other sources of intensity variations could be an offset between the light sheets of the two illumination pulses or fluctuating scattering properties of the particles, e. g. non-spherical particles rotating in the flow.

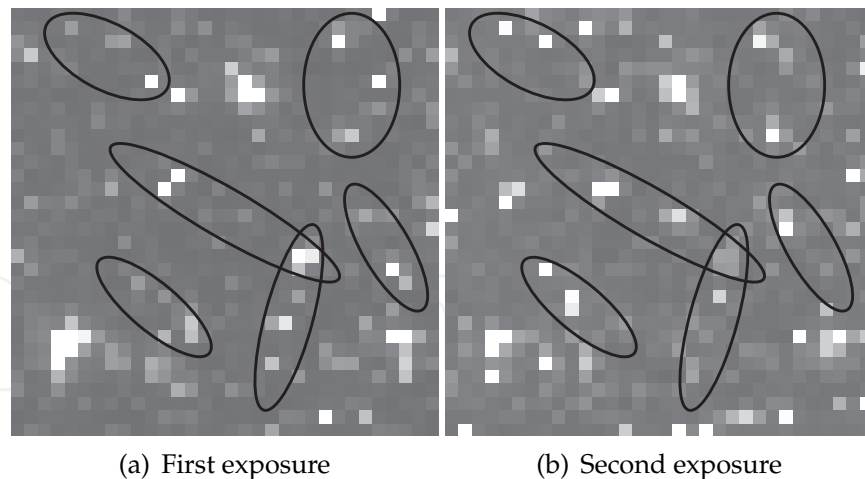(a) First exposure (b) Second exposure

Fig. 2. Examples demonstrating individual particle intensity variations (marked regions, detail of public PIV images from the PIV challenge 2003, case A, axisymmetric turbulent jet in stagnant surrounding, images A001a and A001b)

Note that the effects of intensity variations are different from extern large scale illumination variations (Huang et al., 1997), the intensity variations only due to the different particle locations within the light sheet without relative changes between the exposures (Westerweel, 2000), or the loss-of-pairs and the degradation of the correlation peak due to out-of-plane motion (Keane & Adrian, 1990; 1992; Keane et al., 1995; Westerweel, 2000). While the loss-of-pairs and the degradation of the correlation peak increase the susceptibility to noise and the probability of outliers, the effect discussed here occurs additionally and directly affects the position of the correlation maximum and is a dominant limitation of the achievable accuracy in correlation-based image processing of planar PIV (Nobach, 2011; Nobach & Bodenschatz, 2009).

This study generally applies to Standard-PIV (two-dimensional, two-component, planar), independent of its application. This error principally applies also for Micro-PIV, where the particle images are large and may strongly overlap. However, the particle density and the intensity variations between consecutive images are small yielding a small effect of intensity variations. For Stereo-PIV, the errors are expeted to increase further compared to Standard-PIV due to the necessary coordinate transforms. Furthermore, the errors from the two perspectives are dependent due to the observation of identical particles within the same illumination sheet. In Tomo-PIV a reconstruction of three-dimensional particle locations preceds a three-dimentional correlation analysis. Since the overlap of particle images occurs in the projections only, the three-dimentional correlation should not be affected by this error. However, detailed studies about this error in Micro-PIV, Stereo-PIV and Tomo-PIV are still pending.

2. Effect of varying intensities

In PIV, the displacement of particle patterns between consecutive images is obtained from the peak position in the two-dimensional cross-correlation plane of the two images or image sub-spaces (interrogation windows). Assuming (i) a certain number of imaged particles in

the interrogation window, each with different intensity, but with the same relative intensity in the two consecutive images and (ii) no truncation at the edges of the interrogation windows, the correlation peak is at the correct position, even if the particle images overlap and if the intensity of one entire image is scaled by a constant factor. Note the different meaning of "images", which are the entire images to be correlated, and "particle images", which are the spots at the particle positions. For demonstration, in Fig. 3a two images, each consisting of two well separated particle images (Airy discs), are correlated. The particles are at identical positions in the two images (no displacement between the images). The correct position of the correlation maximum at zero displacement can be seen clearly even for overlapping particle images and also with a constant scaling of one image (Fig. 3b).
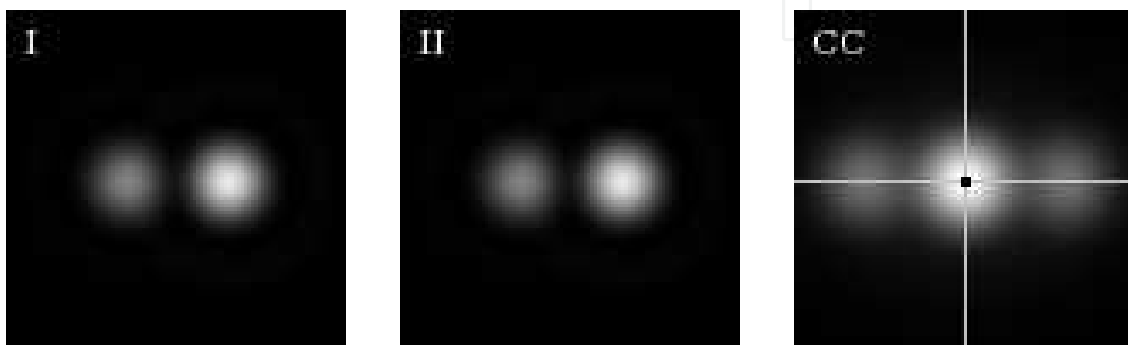
(a) Same intensity of the particle images in the two images with well separated particle images
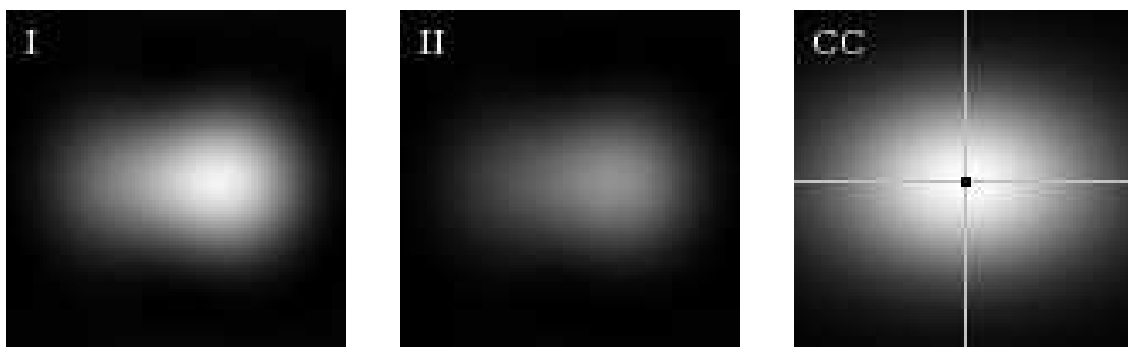
(b) One image intensity scaled and with overlapping particle images

Fig. 3. Intensity and cross-correlation function (CC with lines of zero displacement in x and in y direction respectively and with the correlation maximum marked with a black dot) of two images (I and II), each consisting of two particle images

This holds true also for the correlation of images with different relative amplitudes of the particle images, as long as the particle images do not overlap (Fig. 4a). With overlapping particle images and varying relative amplitudes (Fig. 4b), the maximum position of the correlation peak is shifted, yielding a biased displacement estimate, depending on the amplitudes of the particle images, widths, and overlap.

The consequence for PIV image processing is an additional error in displacement estimates, if the intensities of particle images vary between the consecutive PIV images, while the particle images overlap. This error is especially large for de-focussed particle images (where the particle images tend to overlap) and in the case of misaligned light sheets or flows with
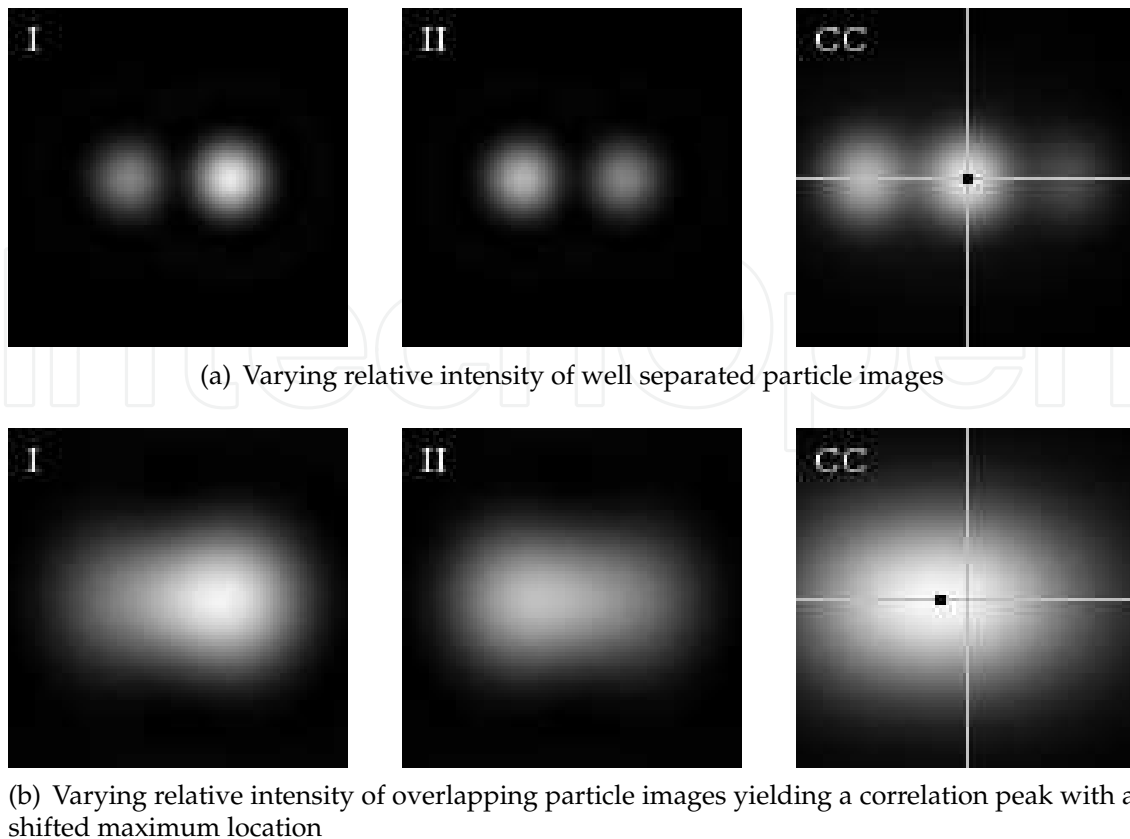
(a) Varying relative intensity of well separated particle images

(b) Varying relative intensity of overlapping particle images yielding a correlation peak with a shifted maximum location

Fig. 4. Intensity and cross-correlation function (CC with lines of zero displacement in x and in y direction respectively and with the correlation maximum marked with a black dot) of two images (I and II), each consisting of two particle images

out-of-plane motion of the particles (where the illumination of individual particles changes between the two light pulses). This is almost independent of the particle number density as shown below.

While different intensities of particle images obviously occur if the particles move out-of-plane in e.g. a Gaussian illumination profile, this effect also occurs for a top-hat profile, if one of the two particle images is present in only one of the images (drop-off), as it occurs if one particle moves out of or enters the illumination plane. With a top-hat illumination profile, the amplitude of one of the particle images stays constant between the two exposures while the other particle image is absent in one of the two images. For well separated particle images (Fig. 5a) the correlation has its maximum at the correct position. As soon as the two particle images (in one of the two images) overlap, the correlation maximum is shifted (Fig. 5b).

3. Accuracy

To derive the dependence of the achievable accuracy on the intensity variations, computer simulated images have been used with varying parameters. The simulated particles are uniformly distributed within the light sheet and over the observation area. To consider the diffraction-limited imaging of small particles, the simulated particle images are represented by Airy functions (diameter given by the first zero value), integrated over the sensitive sensor
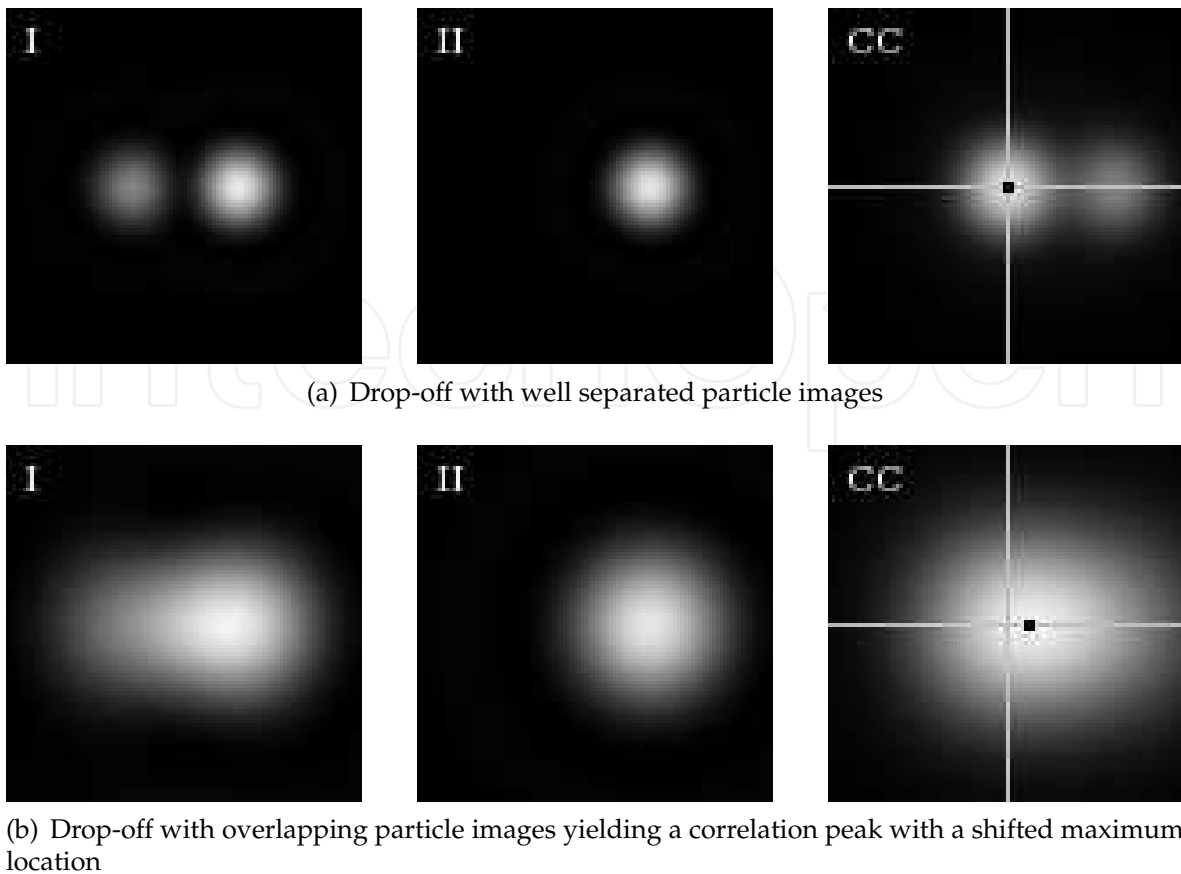
(a) Drop-off with well separated particle images

(b) Drop-off with overlapping particle images yielding a correlation peak with a shifted maximum location

Fig. 5. Intensity and cross-correlation function (CC with lines of zero displacement in x and in y direction respectively and with the correlation maximum marked with a black dot) of two images (I and II), one consisting of two particle images and one with only one particle image (particle image drop-off)

areas (pixels). The pixels are assumed to have a square shape with uniform sensitivity with a fill-factor of 1 (no gaps between the sensitive areas). All particle images get a random maximum intensity, equally distributed between zero and 1000 photo electrons (see comments about the noise below), corresponding to e. g. different sizes or reflectivity. The maximum intensity does not change between the exposures for only in-plane motion. With an out-of-plane motion, the particles change their position relative to the light sheet plane yielding different illumination of each individual particle in the two exposures. In this simulation, a top-hat profile of the light sheet illumination intensity is simulated, where the illumination changes only, if a particle enters or leaves the light sheet. The Airy functions of overlapping particle images are linearly superimposed. To investigate the error of the displacement estimation, a series of 1000 individual image pairs is generated for each of the following test cases. The displacement of the particles between the two exposures is randomly chosen between -1 and $+1$ pixel simulating a variety of sub-pixel displacements. Larger in-plane displacements can easily be eliminated by full-pixel shift of the interrogation windows (Scarano & Riethmuller, 1999; Westerweel, 1997; Westerweel et al., 1997). To isolate the effect of intensity variations from additional effects by e. g. velocity gradients, the simulated displacement is constant for all particles, imitating a homogeneous velocity field.
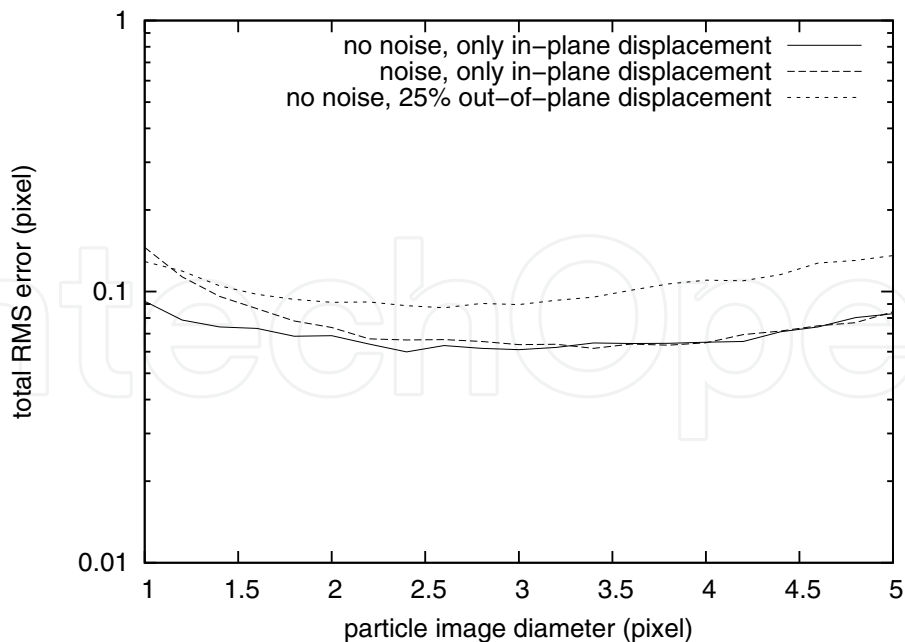
(a) A simple FFT estimation with full-pixel shift
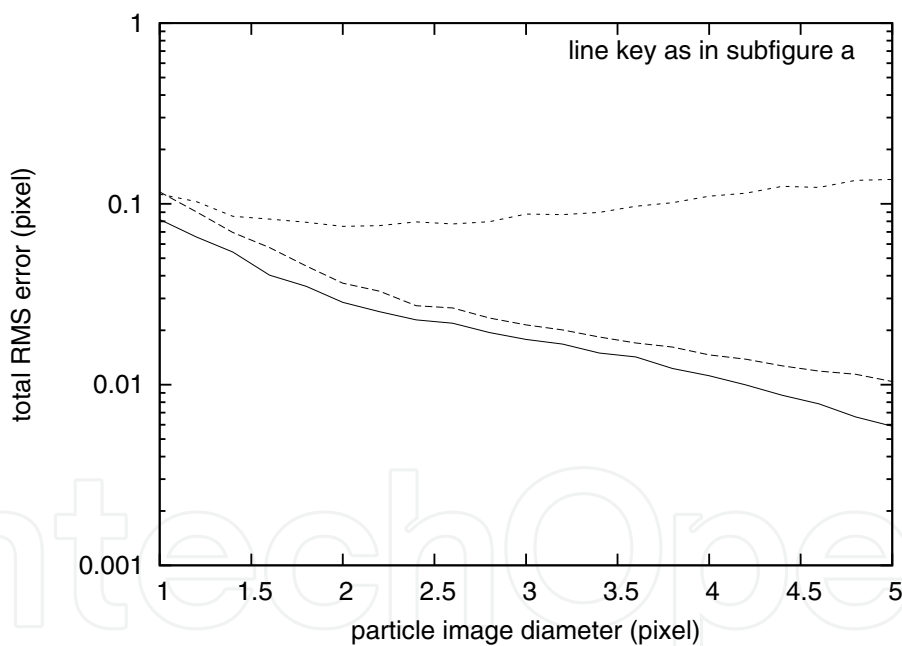
(b) Iterative sub-pixel interrogation window shift with bi-cubic splines image interpolation

Fig. 6. Total RMS error of the displacement estimate as a function of the particle image diameter (particle number density: $0.05 \, \text{pixel}^{-2}$, interrogation window size: 16×16 pixels)

To demonstrate the dominating influence of the intensity variations on the accuracy of correlation-based PIV algorithms, in Fig. 6 the total RMS error over the particle image diameter is shown for three test cases: (i) for only in-plane motion (without noise), (ii) for only in-plane motion, but with strong photon noise (1000 photo electrons for the brightest particles

giving about 32 electrons noise), read-out noise (RMS of 20 electrons) and quantization noise (10 electrons per count, yielding a mean gray value of 102 for the above mentioned 1000 photo electrons incl. read-out noise) and (iii) for an out-of-plane component of 25 % of the light sheet thickness. Fig. 6a shows the results for a simple displacement estimation utilizing the peak position of the cross-correlation of two interrogation windows with 16×16 pixels obtained by means of the fast Fourier transform (FFT). The sub-pixel location of the maximum is obtained by fitting a Gaussian function to the maximum of the correlation and its two direct neighbors in x and y direction separately. In Fig. 6b an iterative window shift method has been used alternatively. Starting with the displacement estimate obtained from the simple FFT-based method above, in the next and all following iteration steps, the two consecutive PIV images are re-sampled at positions shifted symmetrically by plus/minus half the pre-estimated displacement. For re-sampling the images at sub-pixel positions, bi-cubic splines are used for interpolation, widely accepted as one of the best methods so far (Raffel et al., 2007; Stanislas et al., 2008). The interpolation has been realized here with an 8×8 pixels kernel, requiring also the environment of the 16×16 pixels large interrogation window to be simulated. To keep the investigations simple and to isolate the influence of intensity variations, window deformation has not been implemented here to avoid other well known effects, such as limited spatial resolution or dynamic range issues, which may additionally influence the results. However, the conclusions are equally applicable to the case of velocity fields with gradients. In that case the other error sources sum.

The difference between the simulated displacement and that estimated by the above procedures gives individual estimation errors. >From the series of individual errors, an averaged RMS error is derived. In the interesting range of particle image diameters of 2 pixels and larger, for both algorithms, the influence of the out-of-plane displacements is significantly larger that the error due to the noise, making the intensity variations a dominating limitation of the achievable accuracy of planar PIV displacement estimation. The uncertainty of the estimated RMS values is about 21 % of the actual value. This value has been derived assuming independent estimates, yielding an estimation variance of the variance estimate of $2\sigma^4/N$ with N the number of estimates (1000 image pairs) and σ the true RMS value. The uncertainty of the shown graphs is then $\sqrt[4]{2/N}\,\sigma$.

The estimation accuracy can be improved in all three test cases by increasing the size of the interrogation windows, because the displacement errors average (Fig. 7a). The particle image diameter is set fix to 3 pixels. All other simulation and estimation parameters remain unchanged from the simulation above. The results are shown representatiovely for an iterative sub-pixel interrogation window shift with bi-cubic splines image interpolation only. For a constant particle number density, the RMS value decreases as the inverse of the linear dimension of the interrogation window. For large interrogation window sizes a transition towards a lower bound of the total RMS error is indicated. This lower bound is due to remaining interpolation errors in the correlation plane, which are independent of the size of the interrogation windows, and agrees with the findings in Fig. 6.

In contrast, varying the particle number density (Fig. 7b) has almost no effect on the RMS error in the case with an out-of-plane displacement. With only in-plane motion, the number of successfully correlated particle images increases linearly with the particle number density. For each particle, the correlation of the images has a small stochastic error, caused e. g. by image
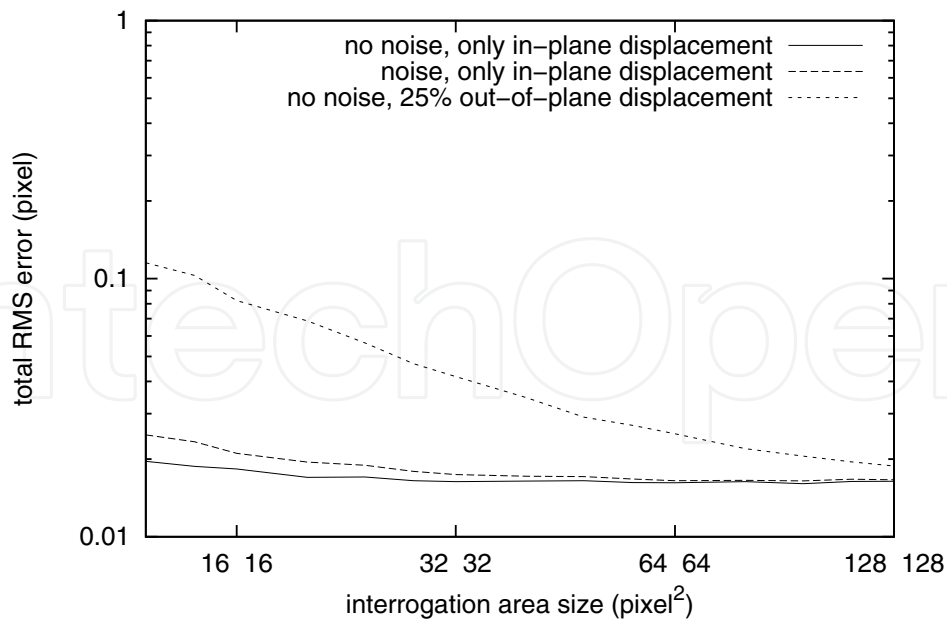
(a) Total RMS error as a function of the size of the interrogation windows
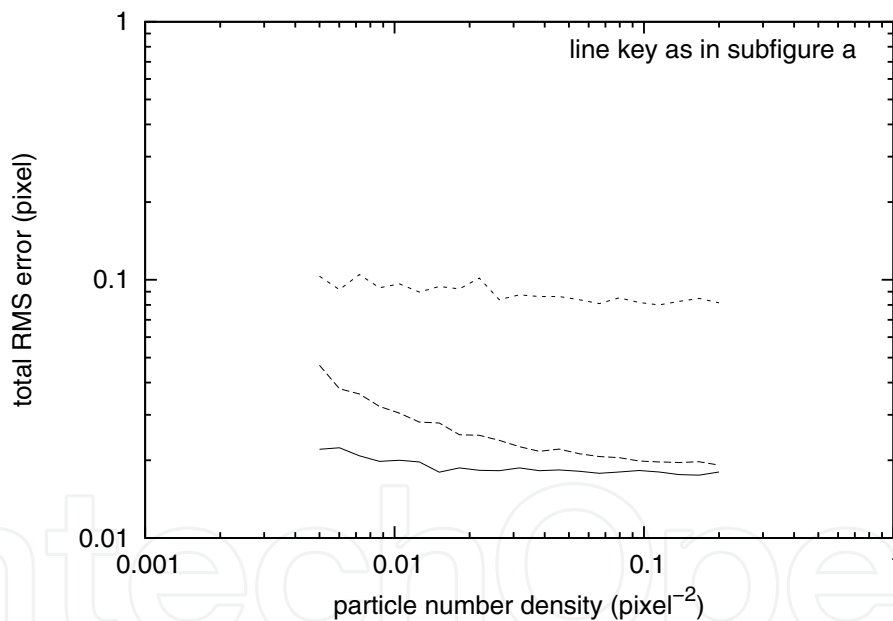
(b) Total RMS error as a function of the particle number density

Fig. 7. Total RMS error of the displacement estimates for an iterative sub-pixel interrogation window shift with bi-cubic splines image interpolation

noise, intensity interpolation over the pixel areas or by errors during image interpolation. The individual errors average over all particles in the interrogation window, yielding an RMS error decreasing with the square root of the particle number density. This complies with Westerweel (2000) (there for low particle densities). This error has a lower bound caused by interpolation errors in the correlation plane, which are independent of the particle number density. The image noise has been used to provoke large RMS errors in Fig. 7b, to make the range of RMS

errors decreasing with the square root of the particle number density on top of the lower bound visible.

If there is a certain out-of-plane displacement, the previous errors are superimposed by the strong influence of intensity variations of overlapping particle images. In contrast to the number of successfully correlated particle images, the probability of overlapping particle images increases with the square of the particle number density. Each of these pairs of overlapping particle images contributes a stochastic error to the correlation. After averaging the individual errors of overlapping pairs of particle images over the number of particles in the interrogation window, these two contributions exactly compensate, and the observed error becomes independent of the particle number density.

A better view onto the influence of the out-of-plane displacement can be achieved by investigating the total RMS error as a function of the out-of-plane displacement (Fig. 8a). Here, a variety of commonly used algorithms has been simulated for comparison: a simple FFT-based estimation with full-pixel shift as above, the same algorithm but with a triangular window function applied to the interrogation windows, a symmetric direct correlation with normalization and iterative sub-pixel shift of the interrogation windows with either bi-linear, Whittaker or bi-cubic splines image interpolation. The different algorithms show the smallest errors for only in-plane motion, however, they have a large variation of achievable accuracy in this case. With increasing out-of-plane displacement, the total error increases approximately exponentially with decreasing difference (on the log scale) between the various algorithms. The large error of the method with the window function applied to the interrogation windows is originated in the smaller "effective" window size, which is for the triangular weighting function about half the nominal size of the window, amplifying the susceptibility to intensity variations. Also the iterative window shift with bi-linear interpolation shows large errors due to the pure quality of the bi-linear interpolation scheme.

For large displacements, also outliers occur. To separate the RMS error due to the limited accuracy and the dominating influence of outliers a simple outlier detection algorithm has been implemented. All displacement estimates outside a range of ± 1 pixel around the expected value are assumed to be outliers and are not taken into account for the calculation of the RMS error. From the number of outliers the probability of outliers is estimated. More reliable outlier detection algorithms based on statistical properties of the surrounding vector field as e. g. in Westerweel & Scarano (2005) could not be used in this simulation because only single displacement vectors are simulated. Starting at about 50 % out-of-plane displacement, the probability of outliers increases rapidly (Fig. 8b), limiting the useful range to a maximum out-of-plane displacement of about half the light sheet thickness for the given particle number density and interrogation window size. For the algorithm making use of the window function the onset of outliers is at smaller out-of-plane displacements due to the smaller effective size of the interrogation window. For the symmetric direct correlation with normalization the onset is shifted to larger displacements due to the better robustness of this procedure. The uncertainty of the estimated RMS values again is about 21 % of the actual value for small out-of-plane displacements ($\sqrt[4]{2/N_1}\,\sigma$, where N_1 is the number of validated estimates) and increases with larger out-of-plane displacements as N_1 the number of validated estimates decreases. The uncertainty of the outlier probability is $\sqrt{P(1-P)/N}$ with the true value P of the outlier probability and N the total number of estimates (1000 image pairs).
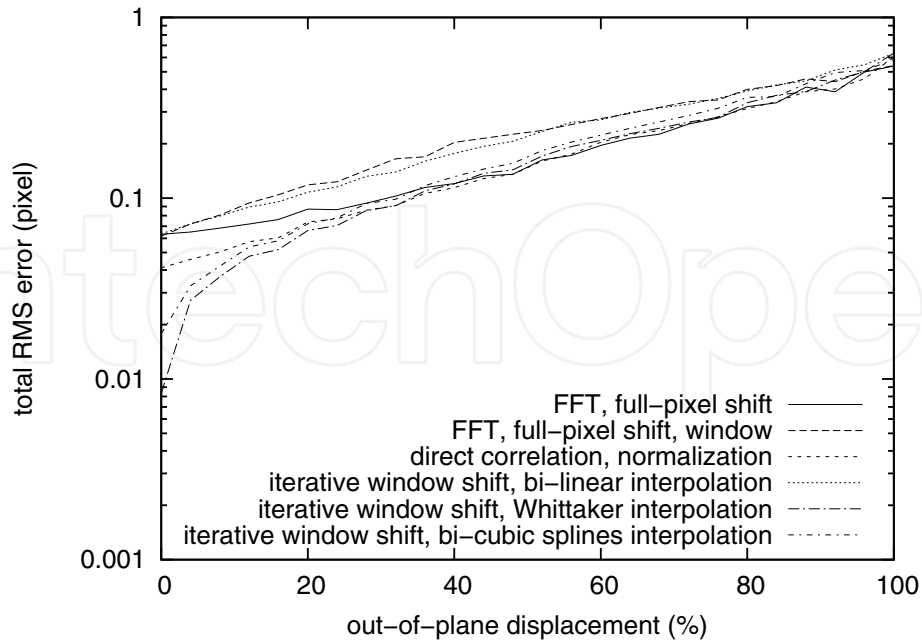
(a) Total RMS error
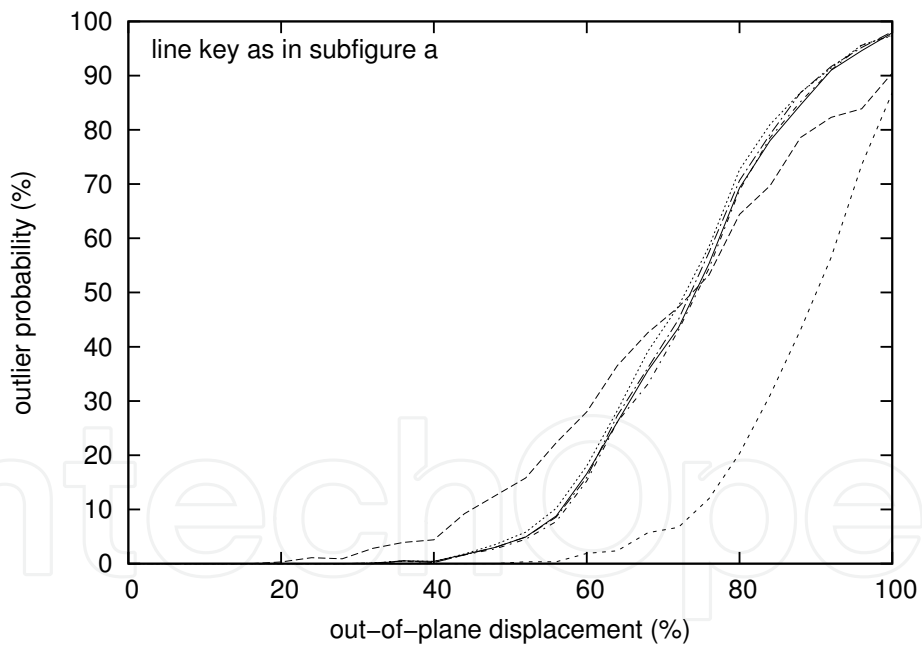
(b) Probability of outliers

Fig. 8. Properties of the displacement estimates as a function of the out-of-plane displacement (in percent of the light sheet thickness) for various PIV procedures (particle number density: $0.05 \, \text{pixel}^{-2}$, interrogation window size: 16×16 pixels)

Experimental verification of the results given above requires a PIV setup with an adjustable beam shape (and width) and an adjustable out-of-plane component of the real velocity field. The first requirement can be realized with a video projector imaging different intensity profiles

into the measurement volume using an additional collimation lens (Fig. 9). To achieve stable illumination, LCD technology is preferred. The projector with DLP technology used here realizes individual gray values by pulse width modulation, which causes illumination problems with PIV cameras at short exposure (integration) times. In the present study the exposure time has been set to 0.25 s, which corresponds to 30 illumination cycles of the DLP chip, since it works at a frame rate of 120 Hz. This long exposure time requires small velocities, which have been realized by moving a solid glass block on a 3D translation stage (Newport CMA12PP stepping motors and ESP300 controller). The glass block has a size of $5 \, cm \times 5 \, cm \times 8 \, cm$ and includes 54 000 randomly distributed dots in the inner $3 \, cm \times 3 \, cm \times 6 \, cm$ volume, corresponding to a particle density of $1 \, mm^{-3}$.
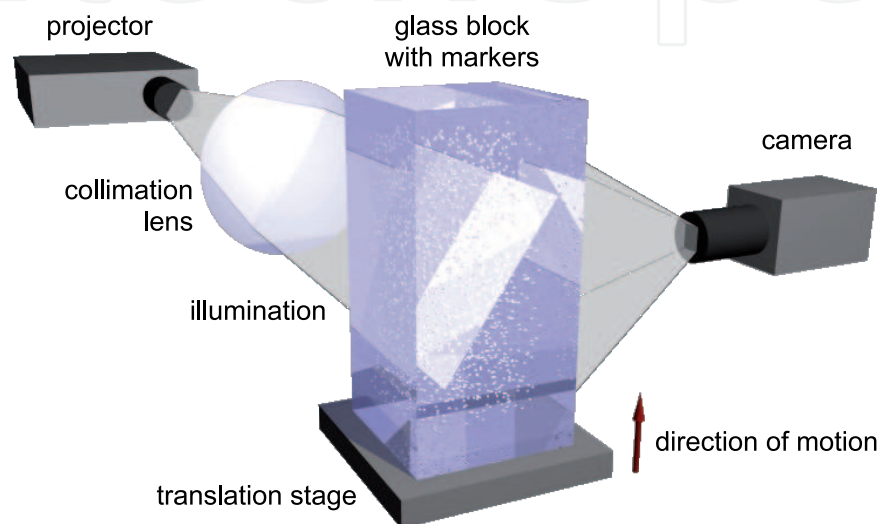

Fig. 9. Sketch of the experimental setup: A video projector is imaging different illumination profiles into the measurement volume, which is observed by a digital camera. A glass block with internal markers is translated vertically through the measurement volume.

Furthermore, an accurate synchronization of the in-plane and the out-of-plane translation through the light sheet is required. To avoid synchronization problems, the system has been inverted. The glass block moves along one axis of the translation stage, while the plane of illumination is tilted with respect to the axis of motion. During the translation of the glass block with a constant velocity of $0.1 \, mm/s$ through the observation area of the camera (Phantom V10), a series of 80 images of 480×480 pixels size has been taken at a frame rate of 0.8 Hz. By choosing the number of frames between the two images to be correlated, different out-of-plane components can be imitated. For details of the experiment see Nobach & Bodenschatz (2009). The images are available from the author. For a comparison to the previous simulation, the images taken with a 4mm wide top-hat illumination profile with a slope of 0.75 have been re-processed in this study.

Unfortunately, the precision of the translation stage and the motion of the glass block are not satisfactory. An *a priory* analysis discovered a frame-to-frame variation of the displacement. Additionally, a small perspective error has been found generating a velocity gradient in y direction. To compensate the displacement variations and the velocity gradient within the observation field, for each image pair, an *a priori* analysis with two large interrogation windows (352×192 pixels) with 50 % overlap in y direction has been taken as a reference
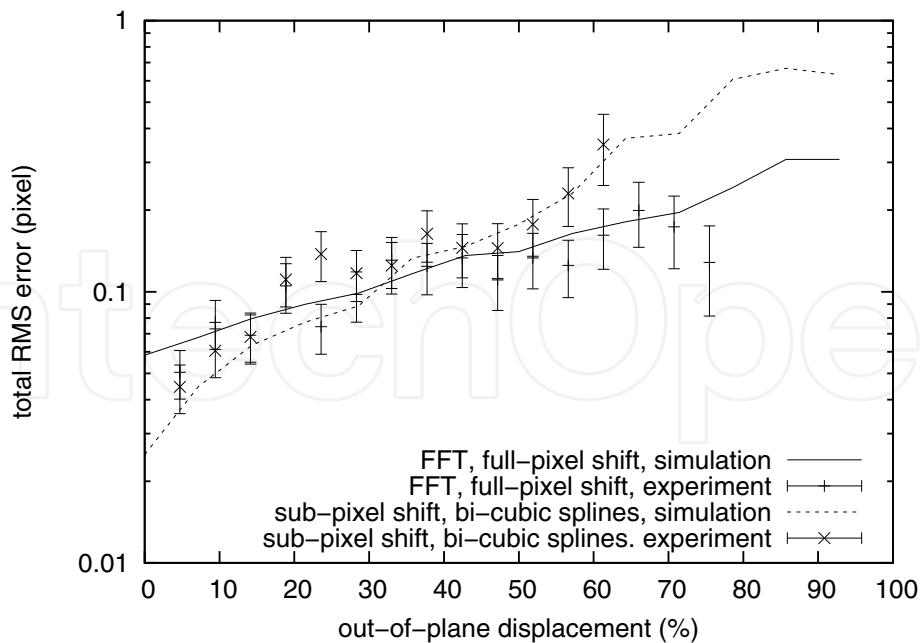
(a) Total RMS error
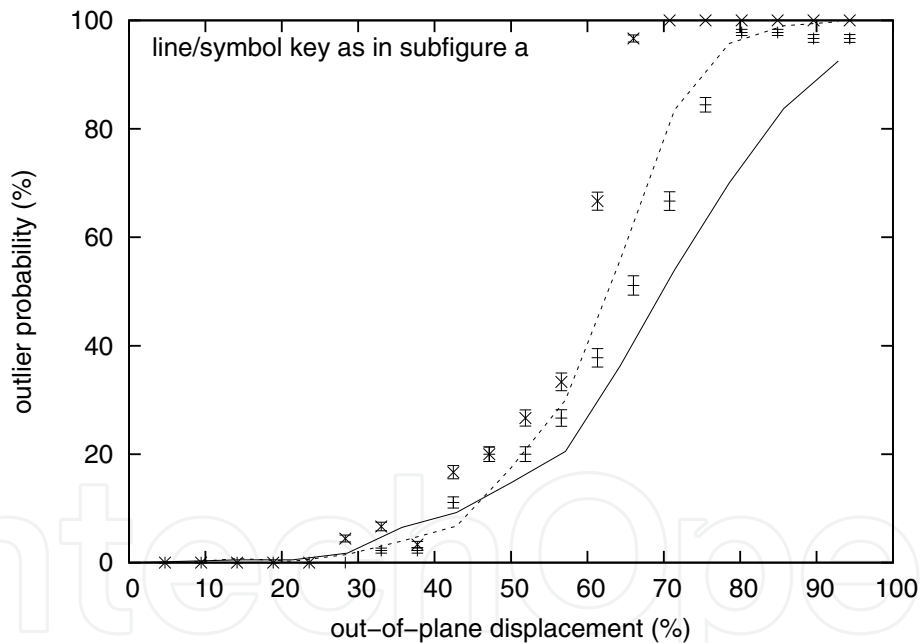
(b) Probability of outliers

Fig. 10. Comparison of the experiment and the simulation for an iterative sub-pixel interrogation window shift with bi-cubic splines image interpolation as a function of the out-of-plane displacement

to derive the mean displacement and the velocity gradients in y direction. The second PIV analysis is done with standard interrogation windows (32×32 pixels) in a 352×288 pixels large window, centered within the original observation area of 480×480 pixels. This area coincides with the area that is taken for the reference estimation. Based on the difference

between the PIV analysis with standard interrogation windows and the reference estimation with large interrogation windows the RMS error is calculated. To suppress effects from the edges, the RMS analysis uses only valid vectors from a further reduced window (160×96 pixels), yielding 5×3 displacement estimates with interrogation windows of 32×32 pixels size. From these estimates the universal outlier detection (Westerweel & Scarano, 2005) can be used as a validation criterion with a threshold of 0.5 pixel plus 2 times the found median RMS derived from the neighboring vectors. For better statistics, all validated displacement vectors from all image pairs with the same number of frames between them, selected from the original series of 80 images, have been averaged.

For direct comparison of the experimental and simulated results in Fig. 10, the numerical simulation has been repeated with simulation parameters and processing and validation methods as for the experimental images (particle number density: $0.013\,\text{pixel}^{-2}$, interrogation window size: 32×32 pixels, iterative window shift and deformation, universal outlier detection). The uncertainty of the results of the simulation again are $\sqrt[4]{2/N_1}\,\sigma$ for the RMS values and $\sqrt{P(1-P)/N}$ for the outlier probability. The pendents for the measurements change with the distance between frames since the number of image pairs decreases with increasing distance between frames. Here error bars are given, showing the interval of plus/minus the RMS of expected uncertainty. Note that the expected uncertainty represents only random errors. Systematic errors or non-detected outliers are not included.

Except for a small shift of large probabilities of outliers towards smaller out-of-plane displacements, the results of simulated and experimentally obtained data agree, verifying both the effect of the intensity variations and the simulation procedure. Remaining deviations are possibly originated in cross-illumination of markers, interference and camera noise.

4. Resolution

To increase the spatial resolution of PIV processing beyond the size of the interrogation windows, overlapping the interrogation windows is an appropriate mean. Of course, this has limitations, since the image data of overlapping windows is not independent, however for moderate overlaps of about $50\,\%$ this works fine for all PIV algorithms, for PIV algorithms with windowing functions or iterative image deformation techniques the overlap can be even larger to obtain further increased spatial resolution. In the latter case, the deformation's degree of freedom is related to the grid of velocity estimates, independent of the interrogation window size. With a high overlap of neighboring interrogation windows the spatial resolution of iterative image deformation is governed by the grid spacing without loosing the robustness of the large interrogation windows. Therefore, this method is gained to improve the achievable spatial resolution of the PIV processing. Instabilities of this technique, occurring for high overlaps of interrogation windows due to negative responses in certain frequency ranges (Nogueira et al., 1999; Scarano, 2004) can be avoided either by applying appropriate spatial filters to the estimated velocity field or the application of appropriate windowing functions to the interrogation windows, which then have frequency responses with only non-negative values. Investigations of stability and spatial resolution of iterative image deformation applying either spatial filters or window functions can be found in Astarita (2007); Lecuona et al. (2002); Nogueira, Lecuona & Rodriguez (2005); Nogueira, Lecuona, Rodriguez, Alfaro & Acosta (2005); Scarano (2004); Schrijer & Scarano (2008).

To proof the gain of resolution by image deformation a series of 100 pairs of PIV images with 512×512 pixels each has been generated with a random in-plane displacement on a pixel-resolution (Gaussian distribution for each component and for each pixel with an RMS value of 0.5 pixel) and no out-of-plane motion. The particle images have random maximum intensities, equally distributed between zero and 1000 photo electrons, and Airy disk intensity profiles with 3 pixels diameter (defined by the first zero value of the Airy disk).

The images have been analyzed with an iterative window shift and first-order deformation technique (Scarano, 2002) with 32×32 and 16×16 pixels window size and an iterative image deformation with a triangular weighting applied to each PIV window of 32×32 pixels size. Except for the interrogation window size, the window function is identical to that in Nogueira et al. (1999), who apply the square of the triangular window to the product of the two PIV windows. To isolate the effect of decreasing the effective window size by weighting, the triangular weighting function has also been applied to the iterative window shift and deformation with a 32×32 pixels window. All methods use 10 iteration and a velocity estimation grid of 8×8 pixels corresponding to 75 % overlap for 32×32 pixels windows and 50 % overlap for the 16×16 pixels window.

>From the individual displacement estimates, which are interpolated with bi-cubic splines and re-sampled at all pixel positions, and the simulated displacement, which originally is given for all pixel positions, a two-dimensional coherent frequency response

$$C_{ij} = \frac{\left\langle U^*_{\mathrm{est},ij} U_{\mathrm{sim},ij} + V^*_{\mathrm{est},ij} V_{\mathrm{sim},ij} \right\rangle}{\left\langle U^*_{\mathrm{sim},ij} U_{\mathrm{sim},ij} + V^*_{\mathrm{sim},ij} V_{\mathrm{sim},ij} \right\rangle} \tag{1}$$

is calculated, where $U_{\mathrm{sim},ij}$ and $V_{\mathrm{sim},ij}$ are the two-dimensional Fourier transforms of the simulated u and the v displacement fields, $U_{\mathrm{est},ij}$ and $V_{\mathrm{est},ij}$ are the estimated counterparts, the * denotes the conjugate complex and $\langle \rangle$ denotes the ensemble average. The products and the coherent frequency function are calculated element-wise for the two-dimensional functions. From the two-dimensional coherent frequency response function a common (one-dimensional) one is derived by iteratively optimizing a one-dimensional function c_i so that the component-wise products $c_i c_j$ fit best the two-dimensional function C_{ij} with minimum L_2 norm.

Fig. 11a shows the frequency response function for only in-plane motion for the four investigated estimation procedures. With a rectangular weighting window, the frequency response clearly drops below zero at $1/32\,\mathrm{pixel}$ or $1/16\,\mathrm{pixel}$ corresponding to the interrogation window size of 32×32 or 16×16 pixels respectively. The triangular weighting window applied to a 32×32 pixels interrogation window leads to a frequency response function with only non-negative values, while the resolution increases beyond the nominal resolution of the interrogation window size, reaching almost an effective window size of half the nominal window size. The image deformation technique can further improve the spatial resolution, which then is limited by the velocity grid of 8×8 pixels. Fig. 12a shows the obtained bandwidth ($-3\,\mathrm{dB}$ limit) as a function of the overlap of interrogation windows. Clearly, the image deformation technique gains most by increasing the density of the velocity estimation grid. Note, that the overlap of interrogation windows for a given grid of velocity estimates
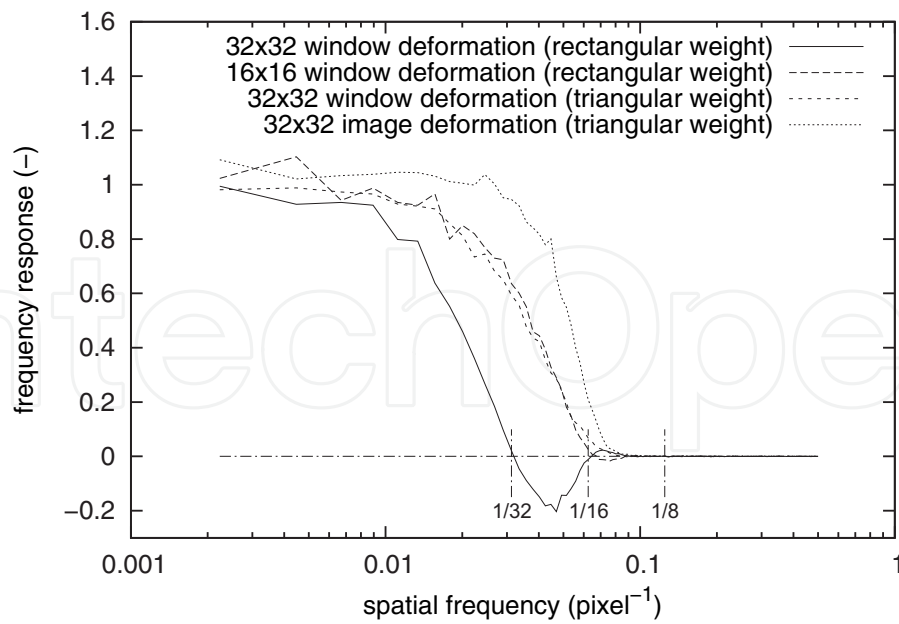
(a) Only in-plane motion
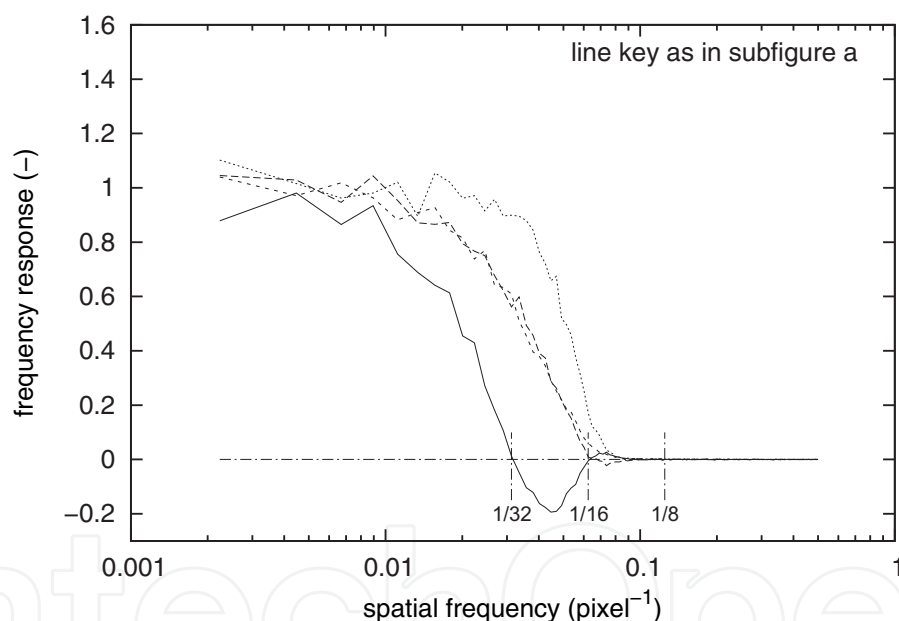
(b) Out-of-plane displacement of 25 % of the light sheet thickness

Fig. 11. Coherent frequency response for the different estimation procedures for a velocity estimation grid of 8×8 pixels corresponding to 75 % overlap for 32×32 pixels windows and 50 % overlap for the 16×16 pixels window (particle number density: $0.05\,\text{pixel}^{-2}$)

changes with the size of the interrogation windows yielding a shifted overlap for the method with the 16×16 pixels interrogation window compared to the other methods.

Figs. 11b and 12b show the corresponding results for an out-of-plane displacement of 25 % of the light sheet thickness. There is no significant difference compared to Figs. 11a and 12a. Therefore, one can conclude that the intensity variations have no significant influence on the achievable resolution.

(a) Only in-plane motion

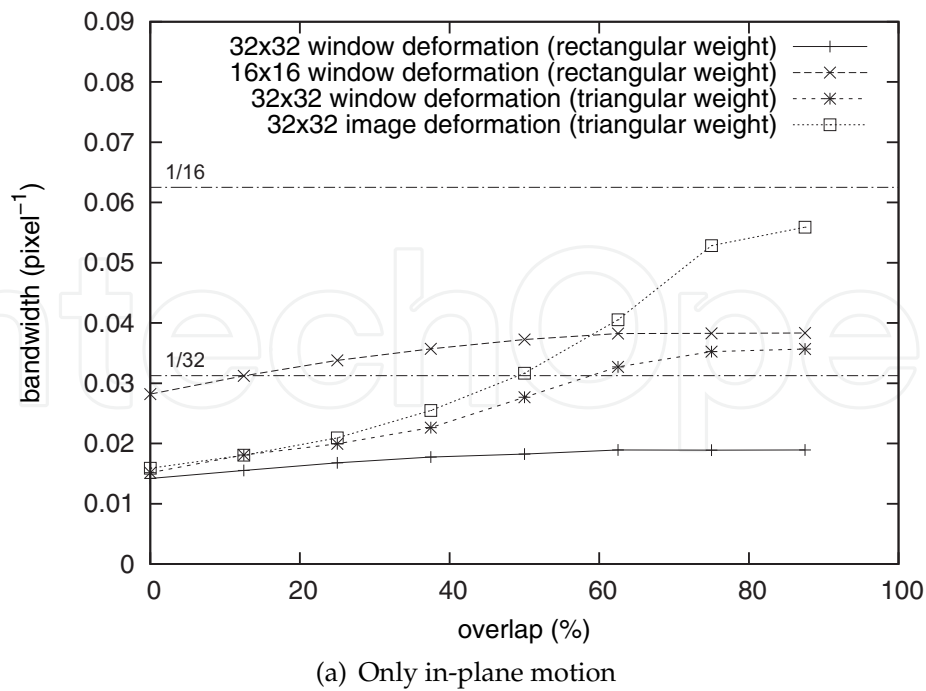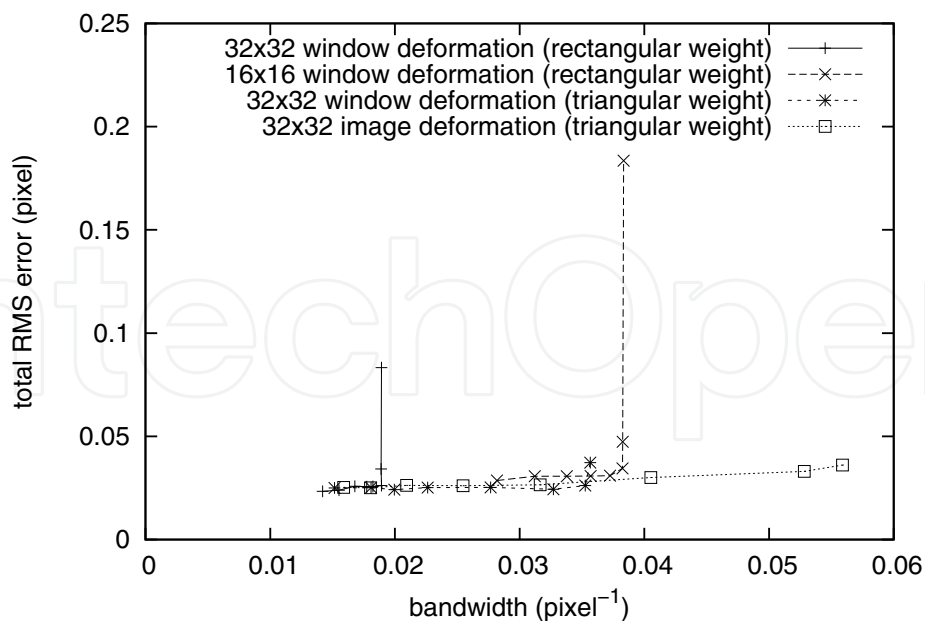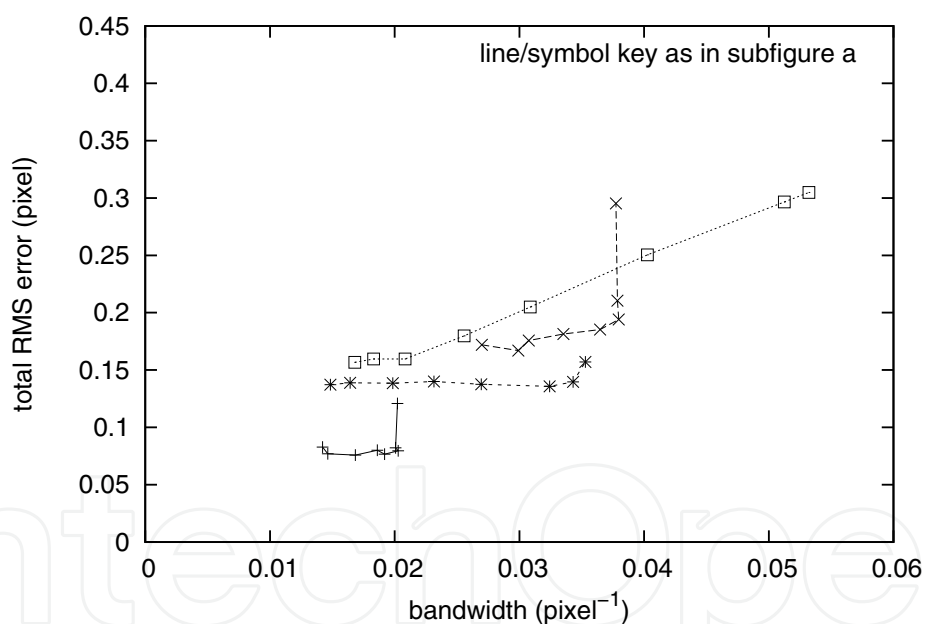(b) Out-of-plane displacement of 25 % of the light sheet thickness
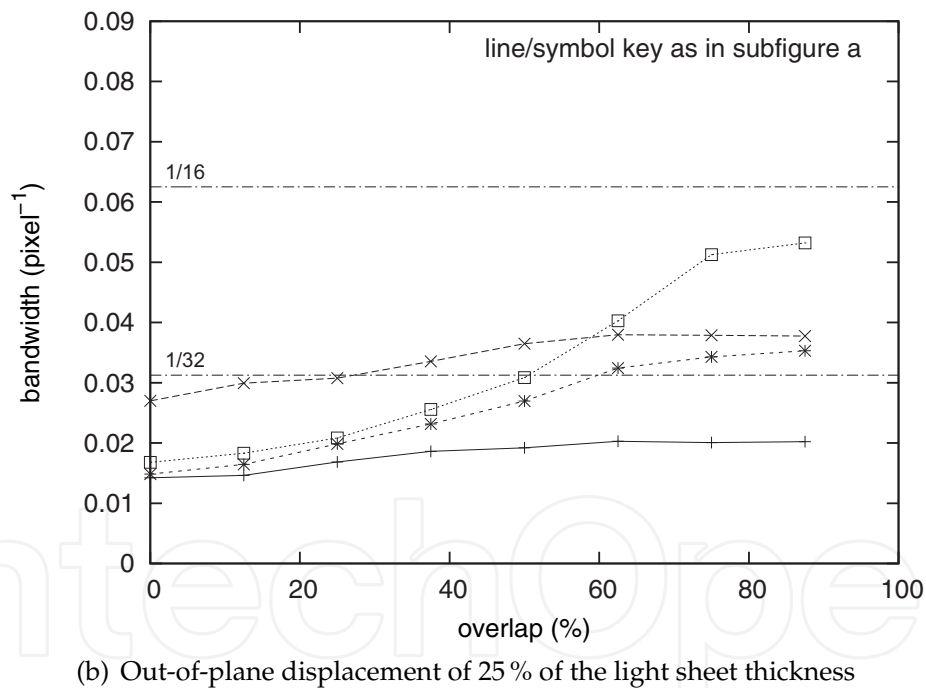
Fig. 12. Bandwidth as a function of the window overlap obtained from a series of simulated PIV images with a random in-plane displacement field (particle number density: $0.05 \, \text{pixel}^{-2}$)

5. RMS error versus resolution

However, taking into account the RMS errors, a significant influence of the intensity variations can be seen. Fig. 13a shows the obtained total RMS errors against the bandwidth with overlaps of interrogation windows varied between 0 and 87.5 %. The various methods cover different

(a) Only in-plane motion

(b) Out-of-plane displacement of 25 % of the light sheet thickness

Fig. 13. Total RMS error against the bandwidth (particle number density: $0.05\,\mathrm{pixel}^{-2}$)

ranges of obtainable bandwidths and RMS errors yielding a lower bound of about 0.02 pixel, slightly increasing with the obtainable bandwidth.

For the window shift and deformation techniques with rectangular window function, the achievable bandwidth basically depends on the size of the interrogation windows. The bandwidth increases slightly with the overlap up to about 50 % overlap. For higher overlaps, the bandwidth stays constant and the RMS error rapidly increases. With the window shift and

deformation technique with a triangular window function the bandwidth further increases up to about 75 % overlap, reaching almost the bandwidth of the window shift and deformation with a rectangular window function of half the size corresponding to an effective window size, which is half as large as the nominal size. Again, the RMS error increases rapidly for further increased overlaps. With the image deformation technique and strong overlap of interrogation windows the bandwidth can be increased further. The RMS error increases much less then with the other methods.

The picture changes completely in the presence of an out-of-plane component. Fig. 13b shows the results for an out-of-plane component of 25 % of the light sheet thickness. Again a rapid increase of the RMS error can be seen beyond 50 % overlap for iterative window shift and deformation techniques with rectangular window functions, respectively 75 % for a triangular window function. The image deformation reaches the highest bandwidth at strong overlaps. However, with the out-of-plane component the errors are much larger than with only in-plane motion and, additionally, the results for the various methods do not overlay any more. For the window shift and deformation techniques the achievable accuracy depends on the window function and the interrogation window size, as one has seen in Fig. 7. For the image deformation, the bandwidth continuously increases with the overlap, and the RMS error nearly linearly increases with the obtained bandwidth, but here for the prize of a larger RMS error in the entire range of overlaps and bandwidths compared to the other methods.

6. Conclusion

The effect of particle image intensities varying individually between the two consecutive images on the obtainable accuracy of a PIV system has been reviewed. Such intensity variations occur in experiments due to the motion of the particles in the intensity profile of the light sheet, misalignments of the two light pulses or changes of the particle's scattering properties between the two exposures. The error has been quantified for several commonly used PIV processing methods. This effect limits the obtainable accuracy of PIV measurements, even under otherwise ideal conditions and is much stronger than noise or in-plane loss of particle images. The commonly used best practice parameters for PIV experiments (particle image diameter around 3 pixels and out-of-plane components of not more than 25 % of the light sheet thickness) and the usually observed limit of about 0.1 pixel could be re-produced. This error is almost independent of the particle number density, but it strongly increases with increasing out-of-plane displacements, and decreases with increasing interrogation window size. In summary, besides under-sampling, the variations of the particle image intensities are an additional error, dominating the range of particle image diameters of larger than 2 pixels. This error leads to a basic limitation of the planar PIV technique and explains the accuracy limit of PIV of about 0.1 pixel usually seen in experiments. High-resolution image deformation techniques as in Nogueira et al. (1999) or Schrijer & Scarano (2008), with their small effective interrogation windows are especially affected in terms of the achievable accuracy, even if the achievable resolution does not change with intensity variations.

7. References

Alexander, B. F. & Ng, K. C. (1991). Elimination of systematic error in sub-pixel accuracy centroid estimation, *Opt. Eng.* 30: 1320–1331.

Astarita, T. (2006). Analysis of interpolation schemes for image deformation methods in PIV: effect of noise on the accuracy and spatial resolution, *Exp. in Fluids* 40: 977–987.

Astarita, T. (2007). Analysis of weighting window functions for image deformation, *Exp. in Fluids* 43: 859–872.

Astarita, T. (2008). Analysis of velocity interpolation schemes for image deformation methods in PIV, *Exp. in Fluids* 45: 257–266.

Astarita, T. & Cardone, G. (2005). Analysis of interpolation schemes for image deformation methods in PIV, *Exp. in Fluids* 38: 233–243.

Chen, J. & Katz, J. (2005). Elimination of peak-locking error in PIV analysis using the correlation mapping method, *Meas. Sci. Technol.* 16: 1605–1618.

Christensen, K. T. (2004). The influence of peak-locking errors on turbulence statistics computed from PIV ensembles, *Exp. in Fluids* 36: 484–497.

Fincham, A. & Delerce, G. (2000). Advanced optimization of correlation imaging velocimetry algorithms, *Exp. in Fluids* 29: S13–S22.

Fincham, A. M. & Spedding, G. R. (1997). Low cost, high resolution DPIV for measurement of turbulent fluid flow, *Exp. in Fluids* 23: 449–462.

Gui, L., Merzkirch, W. & Fei, R. (2000). A digital mask technique for reducing the bias error of the correlation-based PIV interrogation algorithm, *Exp. in Fluids* 29: 30–35.

Huang, H., Dabiri, D. & Gharib, M. (1997). On errors of digital particle image velocimetry, *Meas. Sci. Technol.* 8: 1427–1440.

Huang, H. T., Fiedler, H. E. & Wang, J. J. (1993a). Limitation and improvement of PIV; Part I: Limitation of conventional techniques due to deformation of particle image patterns, *Exp. in Fluids* 15: 168–174.

Huang, H. T., Fiedler, H. E. & Wang, J. J. (1993b). Limitation and improvement of PIV; Part II: Particle image distorsion, a novel technique, *Exp. in Fluids* 15: 263–273.

Jambunathan, K., Ju, X. Y., Dobbins, B. N. & Ashforth-Frost, S. (1995). An improved cross correlation technique for particle image velocimetry, *Meas. Sci. Technol.* 6: 507–514.

Keane, R. D. & Adrian, R. J. (1990). Optimization of particle image velocimeters. Part I: Double pulsed systems, *Meas. Sci. Technol.* 1: 1202–1215.

Keane, R. D. & Adrian, R. J. (1992). Theory of cross-correlation analysis of PIV images, *Applied Scientific Research* 49: 191–215.

Keane, R. D., Adrian, R. J. & Zhang, Y. (1995). Super-resolution particle imaging velocimetry, *Meas. Sci. Technol.* 6: 754–768.

Lecordier, B. (1997). *Etude de l'intéraction de la propagation d'une flamme prémélangée avec le champ aérodynamique, par association de la tomographie Laser et de la Vélocimétrie par Images de particules*, PhD thesis, l'Université de Rouen, France.

Lecordier, B. & Trinité, M. (2006). Accuracy assessment of image interpolation schemes for PIV from real images of particle, *Proc. 13th Int. Symp. on Appl. of Laser Techn. to Fluid Mechanics*, Lisbon, Portugal. paper 26.4.

Lecuona, A., Nogueira, J., Rodríguez, P. A. & Santana, D. (2002). Accuracy and time performance of different schemes of the local field correlation technique., *Exp. in Fluids* 33: 743–751.

Liao, Q. & Cowen, E. A. (2005). An efficient anti-aliasing spectral continuous window shifting technique for PIV, *Exp. in Fluids* 38: 197–208.

Lourenco, L. & Krothapalli, A. (1995). On the accuracy of velocity and vorticity measurements with PIV, *Exp. in Fluids* 18: 421–428.

Morgan, J. S., Slater, D. C., Timothy, J. G. & Jenkins, E. B. (1989). Centroid position measurements and subpixel sensitivity variations with the MAMA detector, *Applied Optics* 28(6): 1178–1192.

Nobach, H. (2011). Influence of individual variations of particle image intensities on high-resolution PIV, *Exp. in Fluids* 50: 919–927.

Nobach, H. & Bodenschatz, E. (2009). Limitations of accuracy in PIV due to individual variations of particle image intensities, *Exp. in Fluids* 47: 27–38.

Nobach, H., Damaschke, N. & Tropea, C. (2004). High-precision sub-pixel interpolation in PIV/PTV image processing, *Proc. 12th Int. Symp. on Appl. of Laser Techn. to Fluid Mechanics*, Lisbon, Portugal. paper 24.1.

Nobach, H., Damaschke, N. & Tropea, C. (2005). High-precision sub-pixel interpolation in particle image velocimetry image processing, *Experiments in Fluids* 39: 299–304.

Nogueira, J., Lecuona, A. & Rodríguez, P. A. (1999). Local field correction PIV: on the increase of accuracy of digital PIV systems, *Exp. in Fluids* 27: 107–116.

Nogueira, J., Lecuona, A. & Rodríguez, P. A. (2001). Identification of a new source of peak locking, analysis and its removal in conventional and super-resolution PIV techniques, *Exp. in Fluids* 30: 309–316.

Nogueira, J., Lecuona, A. & Rodriguez, P. A. (2005). Limits on the resolution of correlation PIV iterative methods. Fundamentals, *Exp. in Fluids* 39: 305–313.

Nogueira, J., Lecuona, A., Rodriguez, P. A., Alfaro, J. A. & Acosta, A. (2005). Limits on the resolution of correlation PIV iterative methods. Practical implementation and design of weighting functions, *Exp. in Fluids* 39: 314–321.

Prasad, A. K., Adrian, R. J., Landreth, C. C. & Offutt, P. W. (1992). Effect of resolution on the speed and accuracy of particle image velocimetry interrogation, *Exp. in Fluids* 13: 105–116.

Raffel, M., Willert, C., Wereley, S. & Kompenhans, J. (2007). *Particle Image Velocimetry — a practical guide*, Springer.

Roesgen, T. (2003). Optimal subpixel interpolation in particle image velocimetry, *Exp. in Fluids* 35: 252–256.

Rohály, J., Frigerio, F. & Hart, D. P. (2002). Reverse hierarchical PIV processing, *Meas. Sci. Technol.* 13: 984–996.

Scarano, F. (2002). Iterative image deformation methods in PIV, *Meas. Sci. Technol.* 13: R1–R19.

Scarano, F. (2004). On the stability of iterative PIV image interrogation methods, *Proc. 12th Int. Symp. on Appl. of Laser Techn. to Fluid Mechanics*, Lisbon, Portugal. paper 27.2.

Scarano, F. & Riethmuller, M. L. (1999). Iterative multigrid approach in PIV image processing with discrete window offset, *Exp. in Fluids* 26: 513–523.

Scarano, F. & Riethmuller, M. L. (2000). Advances in iterative multigrid PIV image processing, *Exp. in Fluids* 29: S51–S60.

Schrijer, F. F. J. & Scarano, F. (2008). Effect of predictor-corrector filtering on the stability and spatial resolution of iterative PIV interrogation, *Exp. in Fluids* 45: 927–941.

Stanislas, M., Okamoto, K., Kähler, C. J., Westerweel, J. & Scarano, F. (2008). Main results of the third international PIV challenge, *Exp. in Fluids* 45: 27–71.

Tokumaru, P. T. & Dimotakis, P. E. (1995). Image correlation velocimetry, *Exp. in Fluids* 19: 1–15.

Utami, T., Blackwelder, R. F. & Ueno, T. (1991). A cross-correlation technique for velocity field extraction from particulate visualization, *Exp. in Fluids* 10: 213–223.

Westerweel, J. (1993). *Digital Particle Image Velocimetry: Theory and Application*, Delft University Press, Delft, The Netherlands.

Westerweel, J. (1997). Fundamentals of digital particle image velocimetry, *Meas. Sci. Technol.* 8: 1379–1392.

Westerweel, J. (1998). Effect of sensor geometry on the performance of PIV interrogation, *Proc. 9th Int. Symp. on Appl. of Laser Techn. to Fluid Mechanics*, Lisbon, Portugal. paper 1.2.

Westerweel, J. (2000). Theoretical analysis of the measurement precision in particle image velocimetry, *Exp. in Fluids* 29: S3–S12.

Westerweel, J. & Scarano, F. (2005). Universal outlier detection for PIV data, *Exp. in Fluids* 39: 1096–1100.

Westerweel, J., Dabiri, D. & Gharib, M. (1997). The effect of discrete window offset on the accuracy of cross-correlation analysis of digital PIV recordings, *Exp. in Fluids* 23: 20–28.

Whittaker, J. M. (1929). The Fourier theory of the cardinal functions, *Proc. - R. Soc. Edinburgh Sect. A Math.* 1: 169–176.

Willert, C. E. & Gharib, M. (1991). Digital particle image velocimetry, *Exp. in Fluids* 10: 181–193.
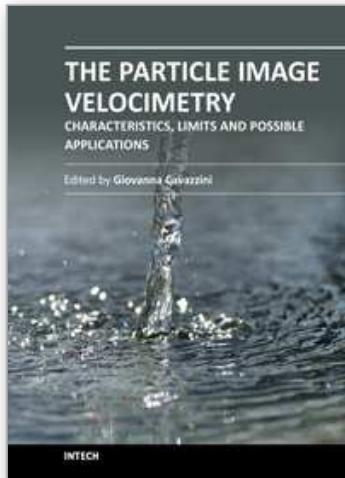
The Particle Image Velocimetry is undoubtedly one of the most important technique in Fluid-dynamics since it allows to obtain a direct and instantaneous visualization of the flow field in a non-intrusive way. This innovative technique spreads in a wide number of research fields, from aerodynamics to medicine, from biology to turbulence researches, from aerodynamics to combustion processes. The book is aimed at presenting the PIV technique and its wide range of possible applications so as to provide a reference for researchers who intended to exploit this innovative technique in their research fields. Several aspects and possible problems in the analysis of large- and micro-scale turbulent phenomena, two-phase flows and polymer melts, combustion processes and turbo-machinery flow fields, internal waves and river/ocean flows were considered.

INTECH
open science | open minds